A 20-year study of melt processes over Larsen C Ice Shelf using a high-resolution regional atmospheric model: Part 1, Model configuration and validation

E. Gilbert[1,2,] †, A. Orr[1], J. C. King[1], I. A. Renfrew[2] and T. Lachlan-Cope[1]

[1] British Antarctic Survey, High Cross, Madingley Road, Cambridge CB3 0ET, United Kingdom.

[2] School of Environmental Sciences, University of East Anglia, Norwich NR4 7TJ, United Kingdom.

Corresponding author: Ella Gilbert (ella.gilbert@reading.ac.uk)

† Present address: Department of Meteorology, University of Reading, Whiteknights Road, Reading RG6 6ET, United Kingdom.

Key words: ice shelves; Antarctic Peninsula; regional climate modelling; surface melt; meteorology; model hindcast

Key Points:

- We present a new high-resolution, multi-decadal hindcast of atmospheric conditions and surface melt processes over the Larsen C ice shelf
- The MetUM hindcast captures the observed location, frequency and interannual variability of foehn events on Larsen C
- The hindcast captures the foehn-induced distribution and interannual variability of surface melt patterns on Larsen C

Abstract

Following collapses of the neighbouring Larsen A and B ice shelves, Larsen C has become a focus of increased attention. Determining how the prevailing meteorological conditions influence its surface melt regime is of paramount importance for understanding the dominant processes causing melt and ultimately for predicting its future. To this end, a new, high-resolution (4 km grid spacing) Met Office Unified Model (MetUM) hindcast of atmospheric conditions and surface melt processes over the central Antarctic Peninsula is introduced. The hindcast is capable of simulating observed near-surface meteorology and surface melt conditions over Larsen C. In contrast with previous model simulations, the MetUM captures the observed east-west gradient in surface melting associated with foehn winds, as well as the inter-annual variability in melt shown in previous observational studies. As exemplars, we focus on two case studies – the months preceding the collapse of the Larsen B ice shelf in March 2002 and the high-foehn, high-melt period of March-May 2016 - to test the hindcast's ability to reproduce the atmospheric effects that contributed to considerable melting during those periods. The results suggest that the MetUM hindcast is a useful tool with which to explore the dominant causes of surface melting on Larsen C.

Plain Language Summary

Scientists are concerned about floating ice shelves on the Antarctic Peninsula because several shelves have collapsed there in recent decades, due partly to melting at the surface. However, our understanding of what causes these ice shelves to melt is limited by the lack of observations in the region, and so numerical models are an extremely useful tool to explore melt processes. This study showcases a new high-quality model dataset that is able to capture the major patterns of surface melting and atmospheric conditions over ice shelves on the Antarctic Peninula. It represents an improvement on previous studies and can therefore be used to examine melt and meteorology on ice shelves like Larsen C. The ability of the hindcast to capture these processes is illutrated via two case studies – the period just before the collapse of the Larsen B ice shelf in March 2002, and a period in March-May 2016 when exceptionally high melt and intense foehn winds were observed on the Larsen C ice shelf. Simulations of reasonable accuracy suggest that the hindcast is suitable for exploring the causes of ice shelf surface melting in the region.

1 Introduction

The Antarctic Peninsula has become a recent focus of attention because of the pace of environmental change there. Changes in the atmosphere and cryosphere have co-occurred: notably, surface warming of up to 3°C between 1951-2000 in the northern Antarctic Peninsula (Turner et al., 2016) coincided with the loss of mass from more than half of the twelve ice shelves surrounding the Antarctic Peninsula since 1947, including the dramatic collapse of the Larsen A and B ice shelves (Cook & Vaughan, 2010). Following a cooling during the 2000s and early 2010s, warming trends have recently resumed (Turner et al., 2016; Bozkurt et al., 2020; Carrasco et al., 2021). The loss or thinning of ice shelves contributes to sea level rise because their ability to buttress upstream grounded ice is reduced, accelerating tributary glaciers and hence the input of ice into the ocean (Rignot et al., 2004, Borstad et al., 2013; Trusel et al., 2015, Fürst et al., 2016).

The collapse of the Larsen A (in 1995) and B (in 2002) ice shelves on the east side of the Antarctic Peninsula was induced by hydrofracturing, whereby water-filled crevasses widen as a result of the hydrostatic pressure acting at the crevasse tip to break apart the ice shelf (Scambos et al., 2000; Kuipers Munneke, 2014). Surface melting is the most important driver of destabilisation via this mechanism because it triggers a series of glaciological processes that begins with firn densification (Scambos et al., 2000; van den Broeke, 2005; Holland et al., 2011). Surface meltwater percolates into the porous firn layer during summer, and once the firn becomes saturated with refrozen meltwater over many seasons, water is forced to collect in surface melt ponds (Scambos et al., 2000; Kuipers Munneke et al., 2014). This leads to hydrofracturing and ice shelves disintegrating extremely rapidly: over about a month in the case of Larsen B (Scambos et al., 2003). The southward progression of ice shelf collapse on the east side of the Antarctic Peninsula indicates that Larsen C, the largest remaining ice shelf in this region, may become unstable in the near future (Rott et al., 1996; 2002; Scambos et al., 2003; Trusel et al., 2015; Bevan et al., 2017).

Larsen C is located at approximately 66°S – 69°S and has an area of ~47,000 km^2. Its climate is dominated by the influence of cold, continental air masses that flow off Antarctica plateau as southerly barrier jets (Parish, 1983). However, foehn winds, which are generated when air is forced over the steep terrain of the Antarctic Peninsula mountains, are also observed over Larsen C between 6-20% of the time, especially during periods of westerly and north-westerly flow (King et al., 2017; Turton et al., 2018; Wiesenekker et al., 2018; Datta et al., 2019; Elvidge et al., 2020). Foehn dramatically alter the local climate and surface energy balance (SEB) for hours or days at a time, generating downward turbulent heat fluxes of the order of 100s of W m^{-2} compared to non-foehn values of 10s W m^{-2}, which are often directed away from the surface (Cape et al., 2015; Elvidge et al., 2015; 2016; 2020; Elvidge & Renfrew, 2016; Kuipers Munneke et al., 2012; 2018). Luckman et al. (2014) and Bevan et al. (2018) used satellite measurements to show that the annual melt duration on Larsen C is highest in the north, where temperatures are closer to the melting point, and in inlets close to the mountains, where foehn winds are most intense and frequent (Turton et al., 2018; Elvidge et al., 2015; 2020). These foehn induced east-west gradients in melt are also seen in borehole and firn measurements (Hubbard et al., 2016; Bevan et al., 2017; Holland et al., 2011).

Foehn flows are associated with both “jet” and “wake” regions over Larsen C, with jet regions downwind of mountain passes being relatively windier-but-cooler and wake regions downwind of mountain peaks being relatively calmer-but-warmer (Elvidge et al., 2015; Elvidge et al., 2020; Orr et al., 2021).

However, despite their importance for inducing melt over Larsen C, a comprehensive long-term estimate of how frequently foehn events occur and their associated impacts on atmospheric conditions and the SEB over the Larsen C ice shelf has not yet been made. Several estimates of foehn frequency have been made using Automatic Weather Stations (AWSs) on the ice shelf (Turton et al., 2018; 2020; Weisenekker et al., 2019; Laffin et al., 2021) or over relatively short time periods of a year or less (King et al., 2017; Kirchgaessner et al., 2019; Elvidge et al. 2020).

Regional climate models have been increasingly used in recent years to assess melting and near-surface meteorology on Larsen C. These models successfully simulate the temperature and solar radiation-driven north-south gradient in melting, but many struggle to reproduce the east-west gradient in melt associated with foehn winds (e.g. van Wessem et al., 2016; Datta et al., 2019). This is largely a result of the use of hydrostatic models or models with insufficient horizontal resolution to adequately simulate the dynamics of foehn winds in complex orography, and therefore its impact on SEB and consequently melting. For example, although Datta et al. (2018 & 2019) find enhanced surface melting and foehn occurrence in inlets on the southern part of Larsen C, it is only found in the strongest foehn cases, resulting in a much weaker east-west gradient in climatological melting than observed. This is perhaps partly because they use the hydrostatic Modèle Atmosphérique Regionale at a spatial resolution of 10 and 7.5 km, which may be too coarse to resolve the complex dynamics of foehn winds on the Antarctic Peninsula.

Recently Elvidge et al. (2020) using the UK Met Office Unified Model (MetUM) at a spatial resolution of 1.5 km became the first study to adequately capture the east-west gradient of foehn-driven melting on Larsen C and, importantly, to explain the drivers of melt in terms of boundary-layer processes affecting the SEB. However, the relatively short (6 month) period considered by that study highlights the need for a comprehensive and long-term (multi-decadal) model dataset that realistically includes the primary atmospheric processes contributing to the SEB and surface melt on Larsen C. This study addresses this need.

Firstly, and most importantly, this study presents a regional configuration of the MetUM at a spatial resolution of 4 km, which is able to resolve the foehn-driven melting over the Larsen ice shelves. Second, the ability of the MetUM to capture the observed spatial gradients and absolute totals of surface melting, and determine the dominant atmospheric drivers of these, will be presented. The fidelity of the hindcast will be examined by evaluating surface melt and foehn occurrence over Larsen C during the main hindcast period 1998-2017, and by simulating two case studies: 1) the Larsen B ice shelf prior to its collapse in 2002, and 2) the Larsen C ice shelf during a concerted period of high melt / high foehn that occurred in 2016 (Kuipers-Munneke et al., 2018). In this paper, we present model-based multi-decadal climatological maps of surface melt and foehn occurrence for Larsen C. Note that analyses of these, including an evaluation of the primary causes of surface melt, will be developed further in a subsequent manuscript.

2 Data and Methods

2.1 Observational data

We use available AWS data from four stations, AWS 14, 15, 17, and 18 (Figure 1). The longest record of any of the stations is from AWS 14, which covers the period January 2009 – December 2017, while AWSs 15, 17 and 18 cover the periods January 2009 – June 2014, February 2011 – March 2016 and November 2014 – December 2017, respectively. AWS 14 and 15 are both located on a flat and homogeneous region of the Larsen C ice shelf, meaning that measurements taken at these stations are representative of a wider area, as demonstrated in King et al. (2015). Conversely, both AWS 17 and 18 are located in inlets at the base of steep topography, where the meteorology is highly localised. AWS 17 sits on the remnant Larsen B ice shelf, in Scar Inlet, while AWS 18 is located in Cabinet Inlet, close to the foot of the mountains in the north-west of the Larsen C ice shelf.

All stations measure the near-surface meteorology (air temperatures, pressure, humidity and wind speeds – with air temperature and humidity interpolated to 2 m and wind speed extrapolated to 10 m) and radiative and turbulent fluxes, from which surface temperature and the SEB can be determined. Turbulent flux estimates were not available from AWS 15 at the time of analysis. The instrumentation used at the AWSs is described in detail in Kuipers Munneke et al. (2012). The turbulent fluxes are calculated using the bulk method, by applying the SEB model of Kuipers Munneke et al. (2009). Corrections are made to the unventilated temperature data to adjust for positive biases in calm, sunny conditions after Smeets (2006) and Smeets et al. (2018), while shortwave fluxes are corrected for the tilt of the sensor according to the routine of Wang et al. (2016).

The SEB is formulated as follows:

$$E_{tot} = LW_{\uparrow} + LW_{\downarrow} + SW_{\uparrow} + SW_{\downarrow} + H_S + H_L + G_S \quad (1)$$

where E_{tot} is the net sum of energy received at the surface, $LW_{\uparrow}$ and $LW_{\downarrow}$ are the surface upwelling and downwelling components of LW radiation, respectively, $SW_{\uparrow}$ and $SW_{\downarrow}$ are the surface upwelling and downwelling components of SW radiation, respectively, and H_S, H_L and

G_S are the surface sensible, latent and ground heat fluxes, respectively. All fluxes are defined as positive when directed towards the surface.

Surface melt energy E_{melt} is defined as in King et al. (2015), as:

$$E_{melt} = \begin{cases} E_{tot} & T_S \geq 0℃ \\ 0 & T_S < 0℃ \end{cases} \quad (2)$$

such that melt only occurs when there is a surplus of energy at the surface (E_{tot} in Equation 1 is positive) and the surface temperature, T_S, is at or above the melting point.

2.2 Reanalysis data

ERA5 reanalysis data (Hersbach et al., 2020) is used to validate the MetUM hindcast. ERA5 is the latest reanalysis dataset from the European Centre for Medium Range Weather Forecasting, with a horizontal resolution of 31 km and hourly temporal output. We use monthly reanalysis averaged by hour of day to compare with the MetUM hindcast.

2.3 Regional climate model description

In this study the MetUM is run in atmosphere-only limited area configuration. The MetUM contains a non-hydrostatic, fully compressible dynamical core, referred to as ENDGAME (Even Newer Dynamics for General Atmosphere Modelling of the Environment), with semi-implicit time stepping and semi-Lagrangian advection. Atmospheric prognostic variables are the dry virtual potential temperature, Exner pressure, dry density and three-dimensional winds, and moist prognostics such as hydrometeors and specific humidity are advected as atmospheric tracers (Walters et al., 2017). Prognostic variables are discretised horizontally on an Arakawa-C grid and a terrain-following hybrid vertical coordinate with Charney-Phillips staggering used in the vertical.

An inner model domain that includes much of the Antarctic Peninsula and surrounding waters (Figure 1) is nested within a global version of the MetUM to dynamically downscale the global model output to higher resolution, as in Orr et al. (2014) and Gilbert et al. (2020). The global model is run using the Global Atmosphere 6.1 configuration (Walters et al., 2017) and has N768 resolution (equivalent to a horizontal resolution of approximately 17 km at mid-latitudes). The inner domain has 70 vertical levels (with 40 below 5500 m), and uses a rotated latitude-longitude grid to maintain a uniform horizontal resolution of 4.0 km. Although Elvidge et al. (2015) argued that a horizontal grid spacing of around 1.5 km was necessary to resolve foehn winds over Larsen C, this argument was based on the previous version of the dynamical core. Recent improvements incorporated in ENDGAME (Wood et al., 2014) have resulted in a more accurate representation of the flow response to orography, meaning a spatial resolution of ~4 km is now sufficient (Gilbert, 2020).

The inner domain runs using the Regional Atmosphere (RA) configuration 'RA1M' as described in Bush et al. (2020), with modifications to the parameterisation of large-scale cloud and precipitation as described in Gilbert et al. (2020). Gilbert et al. (2020) showed that this was the most suitable model configuration currently available for this region. Full details of the model physics and parameterisations used are given in Gilbert et al. (2020) and Orr et al. (2021).

This configuration is limited by a simple zero-layer snow surface scheme that does not allow liquid to penetrate into the snowpack, nor to refreeze (Best et al., 2011). The snow albedo parameterisation is diagnostic, based on the surface temperature (see section S1 of the supplementary material for further details).

Because of the important influence of the mountains (and land-sea interactions – see Orr et al. (2005, 2014)), the default model orography, land/sea mask and coastline were updated. The updated land-sea mask is based on the Scientific Committee on Antarctic Research Antarctic Digital Database coastline, version 7.0 (released January 2016 and available at https://www.add.scar.org/) and does not include the Larsen A and B ice shelves. The orography is based on the Ohio State University Radarsat Antarctic Mapping Project (RAMP) 200 m resolution Antarctic digital elevation model (Liu, 2015), and is converted for use in the MetUM by interpolating the dataset onto the 4.0 km inner domain and applying a 2D 1-2-1 filter with convolution.

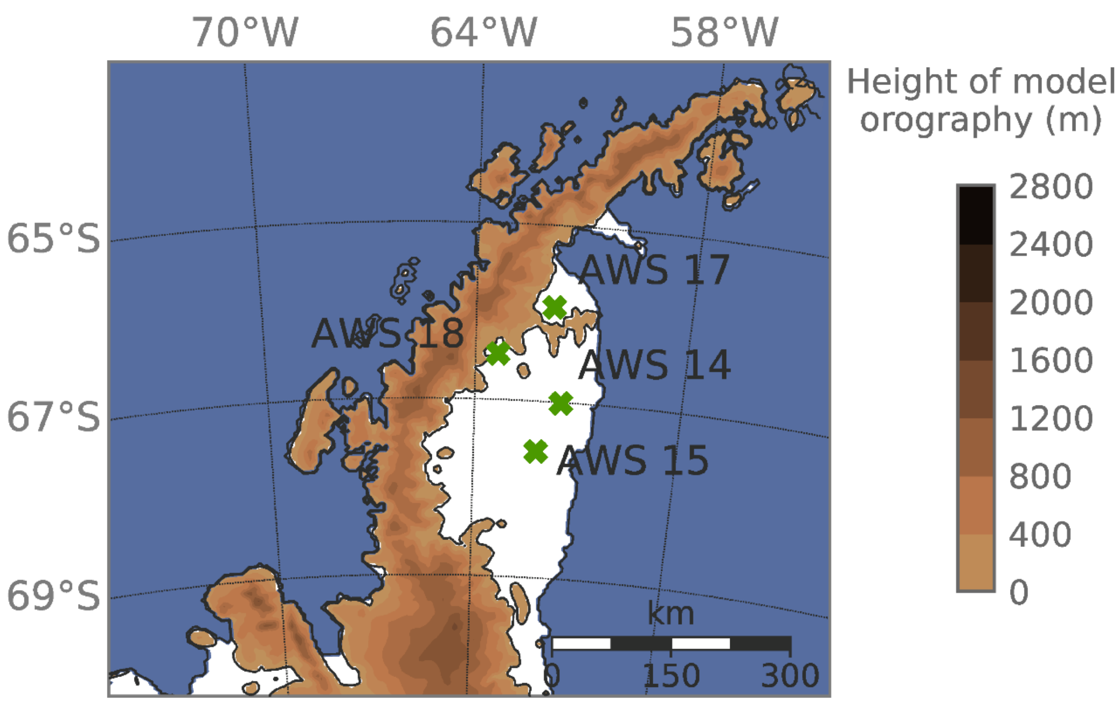

Figure 1. Map of the Antarctic Peninsula MetUM inner model domain with the locations of the four AWSs used for validation indicated with green crosses. The map is centred on the Larsen C ice shelf, on which AWS 14, 15 and 17 are located. The map also shows the remnant Larsen B ice shelf on which AWS 17 is located. The height of the model orography is indicated with coloured contours and is derived from the RAMP 200 m elevation model (Liu, 2015). Ice shelves are shown in white – note the absence of the Larsen A and B ice shelves. Note that an additional shorter run, that focuses on conditions prior to the collapse of Larsen B, uses the same domain but includes both Larsen A and B ice shelves.

2.4 Hindcast set-up

Our main a model hindcast of the northern and central Antarctic Peninsula and Larsen C region is over the period 1 January 1998 to 31 December 2017. An additional shorter run is undertaken to focus on the conditions over Larsen B prior to its collapse, spanning 1 September 2001 – 31

March 2002, and uses a modified land-sea mask that includes both the Larsen A and B ice shelves.

In both the 20-year hindcast and shorter case study run, the global model is initialised from ERA-Interim reanalysis (Dee et al., 2011), and its output is used to provide forcing for the regional climate model / inner domain at 4.0 km horizontal resolution (Figure 1). The model is re-initialised every 12 hours and runs for 24 hours. The first 12-hours are considered spin-up periods and discarded; while the second 12-hour periods are concatenated together to produce a continuous time series. Frequent re-initialisation ensures that the circulation in the inner domain is well constrained and does not drift (Sedlar et al., 2020; Lo et al., 2008), while the discarding of spin-up periods ensures that smaller-scale features are adequately represented. Surface (2D) variables are outputted 3-hourly and 3D variables are 6-hourly, which is considered sufficient temporal resolution to capture key processes such as foehn. Model variables are outputted at the surface (e.g. radiative fluxes), ‘near-surface’ 1.5 m (e.g. relative humidity), 10 m (e.g. winds) or on model levels. Model outputs are validated against available observations and against ERA5 reanalysis.

2.5 Diagnosis of foehn conditions

The occurrence of foehn winds in the model is calculated using two methods that vary in computational expense. To compute the occurrence of model foehn winds at grid points corresponding to AWSs (Tables 3 and 4), an isentrope-based method adapted from the broad-scale approach of King et al. (2017) is adopted, with an additional stipulation that surface warming and/or drying must also be simulated. Whereas King et al. diagnose foehn occurrence across the ice shelf as a whole, in this study the algorithm is used to detect foehn occurrence at each model grid cell. The algorithm is as follows:

- For each model grid cell in which the foehn calculation is being performed, determine the strength of the westerly component of the wind, u, at a location at least one Rossby radius of deformation, λ_R, westwards / upwind of the Antarctic Peninsula. λ_R is calculated as $\lambda_R = Nh/f$, where N is the Brunt-Väisälä frequency, typically 0.01 s^{-1}, h is the height of the mountain barrier, approximately 1500-2000 m on the Antarctic Peninsula, and f is the Coriolis parameter – it is approximately 150 km. The wind is averaged between 250 m and a height Z1 in a manner similar to Elvidge et al. (2015) at the same latitude and the longitude where the distance from the mountains is equal to λ_R. The mean zonal wind within this column is referred to as u_{Z1}, where Z1 is just above the peak height of orography, i.e. it is characteristic of the average westerly flow impinging on the Larsen C ice shelf at the latitude of interest.

- For each model grid point in which the foehn calculation is being performed, if $u_{Z1} \geq 2$ m s^{-1} (and there is therefore a clear west-east cross-barrier flow) then:
    - Find the potential temperature at Z1, θ_{Z1}, and trace this isentrope directly eastwards across the mountain barrier
    - Determine the minimum elevation, Z2, of θ_{Z1} on the lee side of the mountains over Larsen C
    - Determine the maximum change in height of the isentrope θ_{Z1} upwind and downwind of the barrier, i.e. Z3 = Z1 – Z2.
    - For a model grid point, if over any 6 hour period Z3 > 500 m AND 1.5 m air temperature, T_{air}, increases AND 1.5 m relative humidity, RH, decreases, then foehn conditions are detected.

The method is summarised in Figure S1. As this approach is extremely computationally expensive it cannot be used for every grid point in the model domain. Hence, to produce spatial maps of foehn occurrence over the entire Larsen C ice shelf, the method of Turton et al. (2018) was adapted. Turton et al. detect foehn conditions when, over a 12-hour period, one of the following conditions is met:

a) Decrease in RH, below the 10^{th} percentile

b) Decrease in RH below a location-specific threshold

c) Decrease in RH below the 15^{th} percentile plus a 3°C increase in T_{air}

We adopt conditions a) and c), plus include a further stipulation that there be a westerly wind component ($u_{Z1} > 2.0$ m s^{-1}), as above. Sensitivity tests (detailed in section S2 of the supplement) showed that the two methods of identifying foehn events produced comparable results.

It should be noted that the algorithm detects foehn occurrence but not intensity.

3 Results and Discussion

3.1 Model hindcast validation

The MetUM hindcast is validated at all AWSs shown in Figure 1 using all available observations and taking the closest model gridpoint. Missing data are linearly interpolated for validation purposes. Initial inspection of time series at each station (not shown), reveals that AWS 17/18 and AWS 14/15 are similar enough to justify being grouped. The means of the time series at AWS 14/15 and AWS 17/18 are hereafter presented as "ice shelf" and "inlet" stations, respectively. Because the full SEB was not available at AWS 15, ice shelf values for T_S, H_L, H_S, E_{tot} and E_{melt} are taken from AWS 14 only. The full SEB is available at both inlet stations. Table 1 shows observed and modelled annual mean values and the 5th and 95th percentiles for surface variables at ice shelf and inlet stations during the hindcast period. Observed and modelled statistics in Table 1 are given for the observational period available for each station. Scatterplots of observed vs. modelled near-surface variables at AWS 14 during the entire observational period for that station (January 2009 - December 2017) are shown in Figure 2. Validation results at all stations are broadly similar to those for AWS 14, so for brevity, only results from AWS 14 are shown in Figure 2 because it has the longest observational record. These are discussed below.

As also shown by Kuipers Munneke et al. (2018), Gilbert et al. (2020) and Elvidge et al. (2020), the MetUM model at a spatial resolution of 4 km or finer is able to simulate meteorological conditions and consequently the SEB and surface melt over Larsen C in all seasons with reasonable accuracy. This is confirmed by both Figure 2 and Table 1. As shown in Table 1, annual mean T_{air}, T_S, wind speed and RH are positively biased by 2.1°C, 2.4°C, 0.91 m s^{-1} and 2.7%, respectively, at inlet stations and 2.1°C, 3.1°C, 0.81 m s^{-1} and 3.8%, respectively, at ice shelf stations. This makes the MetUM hindcast on average slightly warmer, windier and moister than observations, which is also clear from Figure 2.

The warm bias in air and surface temperatures is likely to be at least partially related to the representation of boundary layer and sub-grid scale turbulent mixing in the MetUM and a documented warm bias in ERA-Interim (Orr et al., 2021; Fréville et al., 2014; Dutra et al., 2015).

T_{air} is consistently more positively biased than T_S in all seasons (Table 1), suggesting that the modelled near-surface temperature gradient is weaker than observed, which may contribute to biases in H_S. Wind, temperature and RH biases may be related to the representation of features and processes such as orography, form drag and surface roughness (Wood & Mason, 1993), the representation of foehn events and foehn jets, the surface and snow schemes, or the influence of the coastline (Orr et al., 2005; 2014; 2021). For example, the representation of topography and surface features in the complex terrain of the Antarctic Peninsula has been shown to strongly influence modelled winds and the simulation of foehn events, which may consequently impact how well temperatures and RH are simulated (e.g. Orr et al., 2008; 2021). Further, Walters et al. (2019) show that the use of the 'zero-layer' MetUM snow scheme produces temperature biases over Greenland, suggesting similar biases may be experienced here.

The inter-percentile range for most variables in Table 1 is captured relatively well by the hindcast, except for RH and H_S. The 5^{th} percentile of observed RH and the 95^{th} percentile of H_S are much lower and higher, respectively, at inlet stations than ice shelf stations due to the effect of foehn winds. However, the hindcast does not capture this completely: the 5^{th} percentile of modelled inlet RH is over-estimated by 7.9% while the 95^{th} percentile of H_S is 7.1 W m^{-2} too large in the model. This is likely caused by the positive temperature bias discussed above.

In Table 1 the daily mean downwelling radiative fluxes are simulated to within 10% of their observed values at all stations and the model SW albedo ($SW_{\downarrow}/SW_{\uparrow}$) is simulated to within 1% and 3% of observed values at inlet and ice shelf stations, respectively. Positive biases in T_S and T_{air} cause $LW_{\uparrow}$ to be over-estimated by 2.9% annually at all stations, generating an energy deficit at the surface (and negatively biased mean net radiation R_{net}, (calculated as LW_{net} + SW_{net}), shown in Figure 2). This contributes to biases in the annual mean of daily mean E_{melt} (Table 1), which is under-estimated by 17-31%. The simplicity of the snow scheme may also contribute to this under-estimation: for example because it does not include sub-surface melting that can occur when the surface is below the freezing point due to the penetration of SW radiation.

Tables S3 and S4 contain additional validation information, showing seasonal statistics for all stations during foehn/non-foehn conditions at inlet (S3) and ice shelf (S4) stations. Negative E_{melt} biases are largest at inlet stations, during December-February (DJF, Tables S3, S4) when the majority of melting occurs, and during foehn events (Tables S3, S4). The exception is during DJF at inlet stations, where the relatively low E_{melt} bias (-0.13 W m^{-2}, Table S3) arises because of compensating biases at AWS17 and AWS18 (-2.26 W m^{-2} and -3.46 W m^{-2}, respectively, during foehn and non-foehn conditions at AWS17 vs. 2.0 W m^{-2} and 0.34 W m^{-2}, respectively, at AWS18). In non-summer seasons, observed and modelled E_{melt} and E_{tot} series are more strongly correlated during foehn, although biases are typically larger, frequently because LW_{net} fluxes are too low and/or T_S does not reach the melting point often enough. This suggests that the hindcast is able to capture the timing of foehn events well, but that the remaining temperature and SEB biases – and potentially errors introduced by the surface scheme - cause the magnitude of E_{tot} and E_{melt} to be under-estimated. This is consistent with previous findings (e.g. Gilbert, 2020) that although the MetUM is able to capture the timing and duration of the foehn cases examined, the magnitude of E_{melt} is under-estimated.

We additionally compare the hindcast against ERA5 reanalysis. Mean values are given in Table 2 for several pertinent variables, including SEB components, albedo, α, and T_S calculated from MetUM output and ERA5 reanalysis over the Larsen C ice shelf. The modelled diurnal cycle of the SEB at inlet and ice shelf stations is also shown for MetUM and ERA5 output in the supplementary material for various seasons (Figures S2 and S3, respectively). Table 2 and Figures S2 and S3 show that there is broad agreement between the MetUM and ERA5. However, the MetUM simulates lower E_{melt} than ERA5 in all seasons except DJF (Table 2), which is consistent with the documented warm temperature bias allowing the surface to reach the melt point more frequently in summer. Figures S2 and S3 show that in DJF ERA5 simulates a slightly positive E_{tot} flux at both inlet and ice shelf stations, whereas the MetUM simulates positive E_{tot} at inlet stations only. This is because H_S, H_L and LW_{net} fluxes - especially around midday - are more negative at ice shelf stations in the MetUM, which results in a higher E_{tot} flux. The DJF E_{melt} flux at inlet stations is much higher in the MetUM than ERA5, likely because of the higher E_{tot} flux and the surface reaching the melting point more frequently (MetUM-simulated T_S is consistently warmer than ERA5 in Table 2). These differences result from the discrepancies in model resolution between the hindcast and ERA5, and demonstrate that the 4 km resolution hindcast is more able to represent foehn events – which we expect in inlets – than the much coarser (31 km) ERA5.

To summarise, at all stations and in all seasons, the hindcast is able to simulate observed surface meteorological variables with reasonable accuracy and to broadly capture SEB components, although E_{melt} is under-estimated, especially during foehn. Many of the biases in SEB terms stem from a warm temperature bias, which is also evident from further comparison with ERA5. However, other errors may be introduced from the surface scheme.

Table 1. Summary statistics for ice shelf and inlet stations in observations and model output. Mean values, as well as the fifth and ninety-fifth percentiles of daily mean surface variables are given, where abbreviations and units are as follows: T_{air}: 1.5 m air temperature (°C); T_S: surface temperature (°C); FF: 10 m wind speed (m s^{-1}); P: surface pressure (hPa); RH: relative humidity

(%); $SW_{\downarrow}$: downwelling shortwave radiation (W m^{-2}), $SW_{\uparrow}$: upwelling shortwave radiation (W m^{-2}); SW_{net}: net shortwave radiation (W m^{-2}); $LW_{\downarrow}$: downwelling shortwave radiation (W m^{-2}); $LW_{\uparrow}$: upwelling shortwave radiation (W m^{-2}); LW_{net}: net shortwave radiation (W m^{-2}); H_S: sensible heat flux (W m^{-2}); H_L: latent heat flux (W m^{-2}); E_{tot}: sum of all (W m^{-2}); E_{melt}: melt flux (W m^{-2}). All fluxes are positive when directed towards the surface.

	Observed						**Modelled**					
	Ice shelf			**Inlet**			**Ice shelf**			**Inlet**		
	Mean	**5th**	**95th**	**Mean**	**5th**	**95th**	**Mean**	**5th**	**95th**	**Mean**	**5th**	**95th**
T_{air}	-15.4	-32.1	-1.5	-14.0	-30.1	0.3	-12.2	-25.7	-1.4	-11.9	-24.9	-1.1
T_S	-14.9	-31.5	-1.2	-14.4	-30.4	-1.1	-12.7	-26.6	-1.5	-12.8	-26.1	-1.7
FF	4.2	1.1	9.2	4.2	1.0	11.2	5.2	2.4	10.1	5.3	1.8	12.1
P	985.0	966.4	1003.9	984.5	965.0	1004.1	983.4	965.0	1002.3	983.0	964.0	1001.7
RH	93.1	80.2	100.0	91.1	65.6	99.1	97.2	83.6	109.0	93.6	73.5	107.3
$SW_{\downarrow}$	128.2	0.3	345.5	126.9	1.3	332.8	124.9	0.0	357.6	124.1	0.0	365.7
$SW_{\uparrow}$	-111.5	-0.1	-289.8	-107.7	-1.2	-276.2	-105.1	-292.4	0.0	-104.1	-297.1	0.0
SW_{net}	18.7	0.0	63.5	19.2	0.1	64.4	19.8	0.0	65.8	20.0	0.0	68.4
$LW_{\downarrow}$	236.1	181.0	295.9	237.8	185.7	293.9	234.0	162.7	298.3	231.5	167.5	293.3
$LW_{\uparrow}$	-254.5	-193.6	-310.3	-256.5	-197.0	-310.5	-262.5	-308.6	-209.3	-261.8	-307.8	-211.0
LW_{net}	-15.7	-47.3	1.2	-18.6	-53.5	1.3	-28.5	-68.3	0.7	-30.3	-66.9	-2.1
H_S	-0.9	-14.8	22.6	3.4	-13.1	47.4	4.0	-11.3	34.3	7.2	-10.7	54.5
H_L	-3.2	-14.0	2.0	-4.2	-14.9	0.9	-1.8	-11.6	4.6	-3.8	-15.2	2.3
E_{tot}	-3.4	-28.4	24.5	-3.4	-29.1	26.3	-6.5	-35.3	18.7	-6.9	-33.7	20.2
E_{melt}	2.7	0.0	19.8	3.4	0.0	24.2	1.8	0.0	13.2	2.4	0.0	15.8

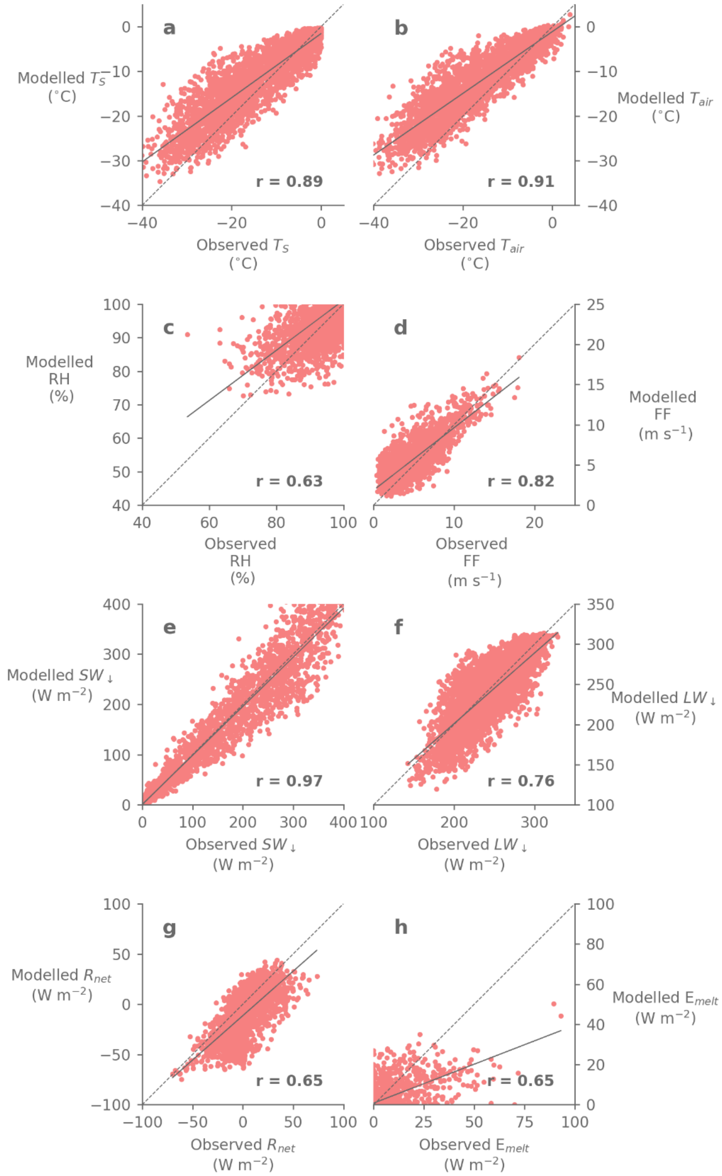

Figure 2. Scatterplots of observed vs. modelled daily means of surface and near-surface variables at AWS 14. Correlation coefficients (r values) are given in the bottom right-hand corner of each panel: all values are statistically significant at the 99% level. The dashed line in each plot indicates perfect agreement between model and observations, while the solid line shows the line of best fit, calculated by a linear least-squares regression. Panels a – d show surface meteorological variables: surface temperature, T_S; near-surface (1.5 m) air temperature, T_{air}; 1.5 m relative humidity, RH; and 10 m wind speed, FF; and panels e – h show surface energy budget terms: downwelling longwave, $LW_\downarrow$; downwelling shortwave, $SW_\downarrow$; net radiative, R_{net} and melt, E_{melt}, fluxes, defined as positive towards the surface.

Table 2. Comparison of mean values of pertinent parameters calculated from daily mean ERA5 reanalysis data and daily mean MetUM output. Data are averaged over the Larsen C ice shelf and shown for each season. Abbreviations are as in Table 1, and with α signifying albedo.

	DJF		**MAM**		**JJA**		**SON**	
	ERA5	MetUM	ERA5	MetUM	ERA5	MetUM	ERA5	MetUM
SW_{net}	57.61	42.87	12.07	6.96	2.66	1.23	31.67	28.51
LW_{net}	-42.42	-31.51	-26.88	-23.77	-27.16	-25.08	-37.18	-32.89
H_S	0.16	0.77	4.39	6.36	8.74	14.31	5.61	7.42
H_L	-8.48	-6.35	-2.99	-0.84	-2.04	0.30	-4.69	-3.30
α	0.85	0.84	0.85	0.85	0.85	0.84	0.85	0.84
T_s	268.28	269.50	257.35	258.47	250.54	250.46	259.30	259.58
E_{tot}	108.35	80.20	34.53	80.18	21.80	79.23	67.92	81.22
E_{melt}	1.57	6.46	0.93	0.24	0.00	0.00	1.43	0.38

3.2 Modelled meltwater production: Larsen C, from 1998 to 2017

Figure 3 shows cumulative annual simulated meltwater production for all full melt years included in the hindcast period (a total of 19 melt years, starting August 1998 and ending July 2017), where melt years are defined as in Bevan et al. (2018) from August-July. Figure 4 shows mean and maximum cumulative annual melt totals for the whole Larsen C ice shelf and shows that mean cumulative melt ranges from 86 mm w.e. yr^{-1} in 2010/11 to 188 mm w.e. yr^{-1} in 2006/07, with maxima simulated in inlets peaking at 1025 mm w.e. yr^{-1} in 2016/17.

The simulated spatial pattern of meltwater production (Figure 3) and number of melt days (Figure S4) is consistent with satellite observations of the annual number of days that surface melting occurs (e.g. Bevan et al., 2018; Luckman et al., 2014), with a clear north-south gradient across the ice shelf, and more melting observed in inlets. The hindcast also simulates peak mean meltwater production during the high melt years identified in Bevan et al. (2018), for example the 2006/07, 2015/16 and 2016/17 melt seasons, when ice-shelf averaged cumulative annual melt of 187 mm w.e., 157 mm w.e. and 161 mm w.e. over 56 d, 48 d and 54 d, respectively, is modelled. The spatial patterns of surface melt shown in Bevan et al. (their Figure 6) are quite closely reproduced in Figure S4, which shows the number of melt days per year. For example more intense melting in inlets during 1999/2000, 2004/05, 2015/16 and 2016/17 is successfully reproduced (when up to 126 d, 115 d, 103 d and 114 d of melting are simulated, respectively); as is the extensive melting during 2006/07 and the relatively limited melting during 2003/04, 2009/10 and 2012/13. Years when melt is shown in the satellite observations but not the hindcast include 2001/02 and 2005/06. The east-west gradient is shown more clearly in melt amount (Figure 3) than in the number of melt days (Figure S4), suggesting that melt intensity is higher in inlets than over the ice shelf. However, the model's ability to reproduce the major patterns of melting, particularly the east-west gradient and the concentration of melting in inlets and the slopes immediately above is extremely encouraging and further justifies the use of the MetUM as a tool for studying this region.

Simulated mean annual meltwater production amounts over Larsen C (Figure 3, Table 2) are also comparable to those derived by Trusel et al. (2013), who used satellite data and modelling to find ice-shelf integrated mean meltwater production of 220 mm w.e. yr^{-1} over the period 1999-2009, exceeding 400 mm w.e. yr^{-1} in the north-western inlets, and Trusel et al. (2015) who show contemporary melt rates over Larsen C of ~300 mm w.e. yr^{-1}. Comparable hindcast-simulated values for 1998-2017 are 132 mm w.e. yr^{-1} for all of Larsen C, and 536 mm w.e. yr^{-1} for inlets only, taking maximum meltwater production rates as a proxy for inlet melting (maxima are always observed in inlets). This suggests that the MetUM may under-estimate surface melting when averaged across the whole ice shelf, consistent with the results shown in Section 3.1. Part of this may be explained by the simple zero-layer snow model and diagnostic albedo implementation. Further, the intensity of foehn flow may not be fully captured by the model, which would impact the amount of melting in inlets.

Although the ice-shelf-mean meltwater totals do not compare exactly in absolute terms with the values reported in Trusel et al., the distributions in Figures 3 and S4 do compare reasonably well with e.g. Bevan et al. (2018). Further, it is notable that maximum values simulated in the north-western inlets during high melt years (up to 797 mm w.e., 602mm w.e. and 1025 mm w.e. in Mill Inlet, on the south-west of Larsen C, during 2013/14, 2015/16 and 2016/17, respectively, and up to 780 mm w.e. in Cabinet Inlet (the location of AWS 18), in the north-west, during

2006/07) exceed the ~725 mm w.e yr^{-1} observed over Larsen B before its collapse (Trusel et al., 2015).

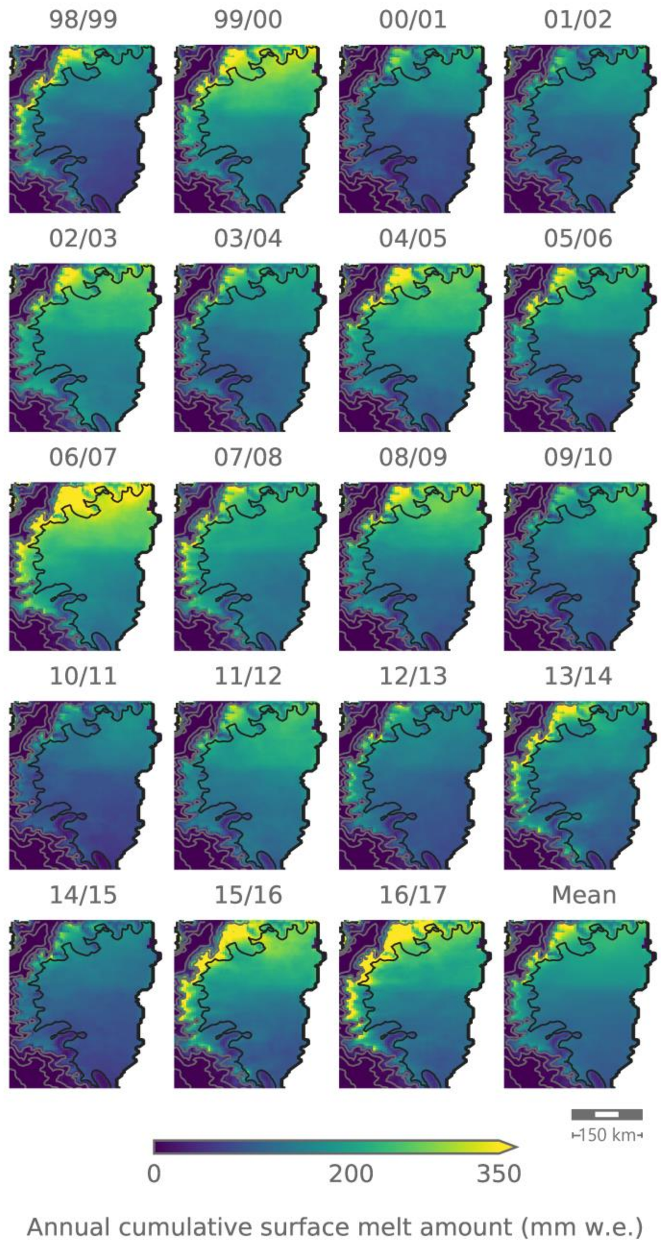

Figure 3. Total annual cumulative snow melt amount (in mm meltwater equivalent per year, mm w.e. yr^{-1}) across the Larsen C ice shelf for each melt year (August - July, defined as in Luckman et al., 2014 and Bevan et al., 2018) in the period 1998-2017. The 50 m elevation contour, approximately the height of the modelled ice shelf at the grounding line, is shown in black, and additional elevation contours at 500 m intervals are shown in light grey. The bottom right subplot shows the mean annual cumulative snow melt amount for all melt seasons.

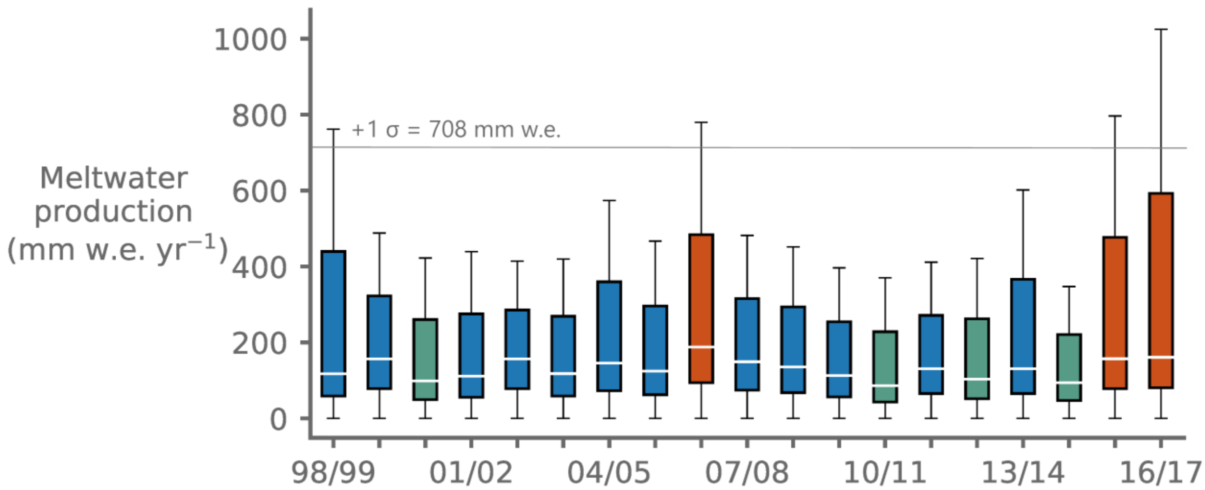

Figure 4. Box-and-whisker plot of modelled annual meltwater production (in mm w.e. yr^{-1}) over the Larsen C ice shelf and tributary glaciers during each melt year (August-July) in the hindcast period. The median meltwater production totals over the whole ice shelf for each melt year are shown as white lines, the boxes show the interquartile range and the whiskers show the minimum and maximum values. Years when the median melt amount exceeds +1 standard deviation above the median are shown in dark orange, while years where median melt amount is less than -1 standard deviation below the median are shown in green. The horizontal line shows maximum meltwater production +1 standard deviation above the median for the whole period.

3.3 Modelled meltwater production: The 2001/02 melt season, prior to the break-up of Larsen B

Having established that the MetUM is able to realistically simulate the magnitude and spatial patterns of surface melting observed on the Larsen C ice shelf, we now consider as a case study the period immediately preceding the collapse of Larsen B. Figure 5 shows the cumulative melt amount simulated over the seven-month time period prior to Larsen B's collapse, from the additional shorter hindcast for the period 1 September 2001 – 31 March 2002 (with the Larsen B ice shelf still intact). Mean cumulative surface melt of 340 mm w.e. is modelled across the Larsen B ice shelf during 1 September - 15 February (when Larsen B began to disintegrate), peaking at 664 mm w.e. in the foot of the mountains (Figure 5). This magnitude of melt is comparable to the value of ~725 mm w.e. yr^{-1} reported by Trusel et al. (2015) to have been observed prior to its collapse. Particularly, melting in inlets close to the grounding line (approximately in the vicinity of the 50 m elevation contour given in Figure 5) could have destabilised the ice shelf in a critical area. Melt-induced thinning in the vicinity of the grounding line has been shown to reduce ice shelf buttressing capacity more considerably than elsewhere on the shelf (Khazendar et al., 2016).

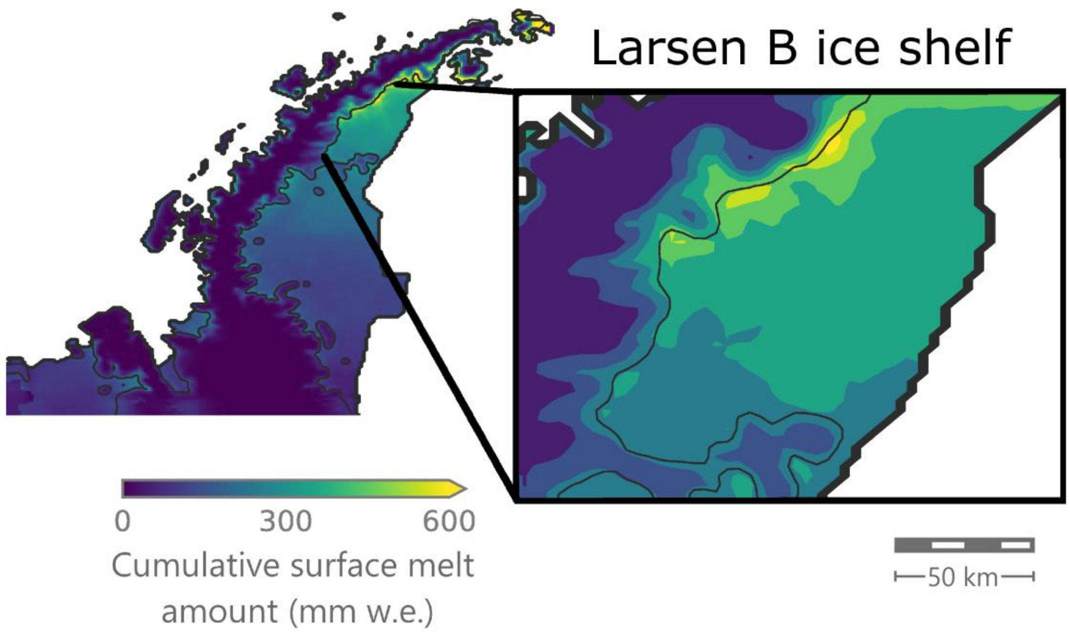

Figure 5. Cumulative surface melt amount simulated during the period 1 September 2001 – 15 February 2002 over the Antarctic Peninsula domain (with the Larsen B ice shelf still intact, main figure) and zoomed in over the Larsen B ice shelf only (inset). The 50 m elevation contour is shown in both plots as the black contour.

The ability of this model run to capture the causes of this extensive melting are next examined. In the simulation, the majority of melting occurred mid-November - February, with sustained daily mean modelled ice-shelf melt fluxes and meltwater production of 8.4 W m^{-2} and 2.2 mm w.e., respectively. Van den Broeke (2005) reports that the 2001/02 melt season was three times longer than the average of the preceding five summers because of the synoptic conditions, which established anomalously low sea ice concentrations in the Weddell Sea (east of Larsen B) and strong foehn flow. Figure 6a shows the mean modelled meteorological conditions across the entire Antarctic Peninsula domain, and over Larsen B (Figure 6b) during the period 10

November 2001 – 1 March 2002. During this period, the melt point was frequently reached (not shown), allowing melting to occur, especially in a narrow band along the foot of the mountains in the northwest of the ice shelf, where T_{max} was also frequently above 0°C (Figure 6b).

Low wind speeds (<3 m s^{-1}) over Larsen B and strong upwind westerly flow caused by an anomalously deep Amundsen Sea Low suggests that foehn were important in producing higher surface melt fluxes. This is also suggested by Cape et al. (2015), who show a strong correlation between the monthly mean number of melt days and monthly mean foehn frequency anomaly over Larsen B during this period, and is further supported by the negative and positive mean H_L and H_S, respectively, shown in Figure 6c and 6d. Large negative and positive H_L and H_S fluxes of the order of 100s W m^{-2}, respectively, are simulated in the lee of mountains upstream of Larsen B, suggesting an influx of warmer, drier air produced by foehn flow. During this period, this generates mean E_{tot} fluxes averaged across Larsen B of 32.0 W m^{-2}, driving melt whenever surface temperatures exceed the melting point.

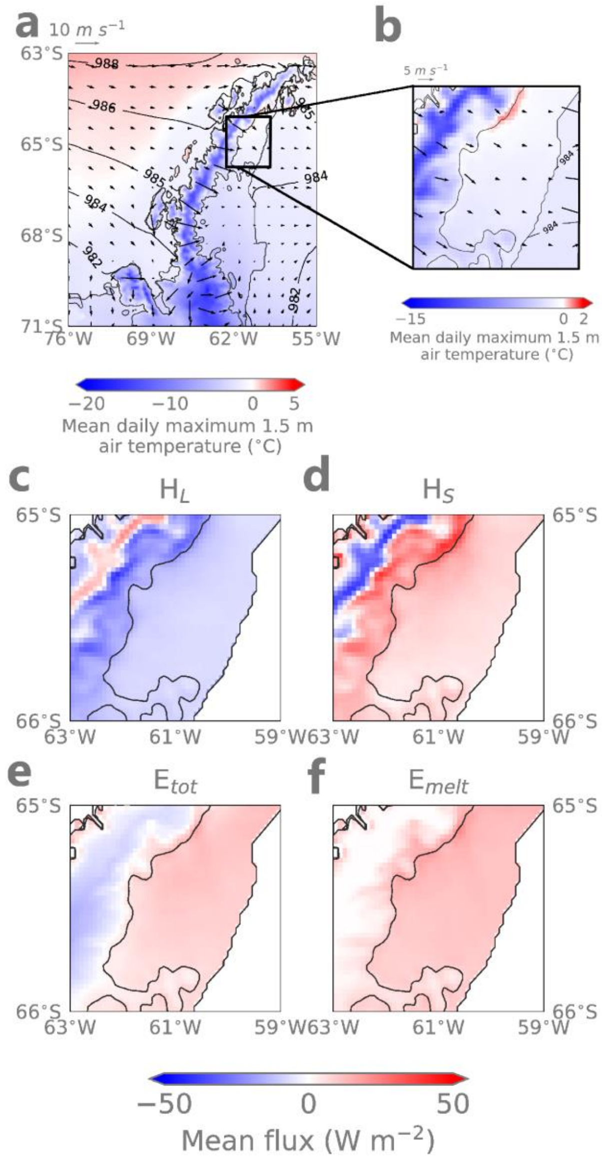

Figure 6. Mean modelled synoptic meteorological conditions and SEB components during 10 November 2001 - 1 March 2002, when excessive melt was occurring over Larsen B prior to its breakup. Panels a) and b) show mean meteorological conditions, where coloured shading shows the mean daily maximum 1.5 m air temperature throughout this period, and contours and vectors give mean sea level pressure and 10 m winds, respectively. Note that the land-sea mask includes the Larsen A and B ice shelves. Mean conditions are shown in panel a) while the inset (panel b) shows conditions over the Larsen B ice shelf only. Note that the temperature and wind speed scales are altered in the inset to show more detail. Panels c) - f) show mean surface energy fluxes (H_L, H_S, E_{tot} and E_{melt}, respectively) over the Larsen B ice shelf, in units of W m^{-2}.

3.4 Frequency of foehn events: Larsen C, from 1998 to 2017

The frequency of foehn events at inlet and ice shelf stations is diagnosed using the isentrope-based method detailed in Section 2.5. Table 3 shows summary statistics (mean, median and standard deviations) of foehn occurrence at inlet and ice shelf stations for the hindcast period, decomposed into seasons, and given as an annual average. The modelled spatial distribution of foehn occurrence across the Larsen C ice shelf is shown in Figure 7, computed using the method of Turton et al. (2018) detailed in Section 2.5.

Consistent with previous studies (e.g. Turton et al., 2018; Wiesennekker et al., 2018; Datta et al., 2019; Elvidge et al., 2020) the highest foehn frequencies are simulated in the immediate lee of steep elevation, with foehn events occurring on average 16% of the time annually at inlet stations and 13% of the time at ice shelf stations (Figure 7, Table 3), comparable values to those cited in the aforementioned studies. A clear gradient is evident in Figure 7 with foehn frequency declining with distance from the mountains. The gradient is qualitatively similar to the gradient in surface melting shown in Figure 3, with higher melt simulated in the northwest and in inlets, suggesting a key role for foehn in causing surface melt (see also Elvidge et al., 2020). The importance of foehn in driving melt will be evaluated in Part 2 of this study. Foehn events are most common during September-October-November (SON) at all locations and standard deviations are highest in DJF and March-April-May (MAM), indicating higher inter-annual variability in foehn occurrence in these seasons (Table 3). In recent years, unusually high foehn-driven surface melting has been reported in non-summer seasons, particularly MAM 2016 (Kuipers Munneke et al., 2018). This finding is discussed in detail in the next subsection.

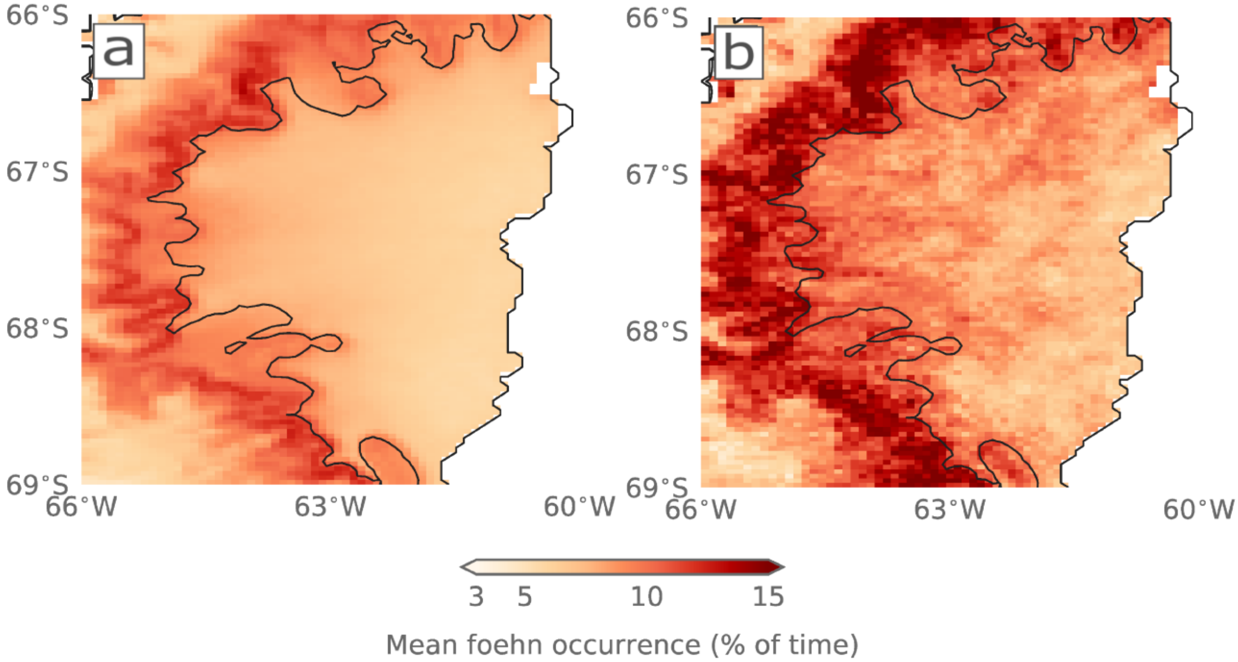

Figure 7. Annual modelled foehn occurrence over the Larsen C ice shelf for a) the full hindcast period 1998-2017 and b) MAM 2016. Foehn occurrence is shown as the mean percentage of time over the period where foehn conditions are diagnosed over Larsen C.

Table 3. Seasonal and annual foehn frequency statistics for ice shelf and inlet stations on the Larsen C ice shelf over the period 1998-2017. Means and standard deviations ("SD") are given for each season and annual totals. Values are calculated from hindcast output using the isentrope-based method described in section 2.5.

		Mean	**SD**
Ice shelf	DJF	11.2%	3.7%
	MAM	12.1%	3.9%
	JJA	13.4%	3.3%
	SON	14.5%	3.1%
	ANN	12.7%	2.4%
		Mean	**SD**
Inlet	DJF	15.4%	4.0%
	MAM	15.4%	3.7%
	JJA	16.1%	3.0%
	SON	18.5%	2.7%
	ANN	16.1%	1.9%

3.5 Frequency of foehn events: Larsen C, MAM 2016

Unusually frequent and intense foehn flow was simulated in the hindcast during the second half of MAM 2016 (Table 4, Figures 7b and S5), the period also examined in Kuipers Munneke et al. (2018). As shown in Figure 7b, foehn frequencies exceeding 20% of the time are simulated in several inlets. Only two years of observations were used in the Kuipers Munneke et al. study, which made it difficult to determine how anomalous these conditions were. However, two more recent studies, Wiesenekker et al. (2019) and Datta et al. (2019), examine this period in the context of longer model runs, satellite and AWS data. These studies, as well as the 20 years of hindcast data presented here make it possible to contextualise these findings.

Mean meteorological conditions during 15 April – 31 May 2016 are shown in Figure 8a. Strong cross-peninsula flow is simulated and mean near-surface daily maximum air temperatures are 5.8°C warmer than climatology for the period, causing surface temperatures to frequently reach the melting point and for air temperatures to climb as high as 12.6°C in Mill Inlet on the 25 May 2016 (the peak of the case identified in Kuipers Munneke et al., 2018).

This synoptic situation permits foehn to occur and perturb the SEB. Panels b – f in Figure 8 show mean anomalies for individual SEB components during 15 April – 31 May. Increased surface temperature produces modest negative $LW_{\uparrow}$ and LW_{net} anomalies (Figure 8b) but the turbulent fluxes differ considerably from the climatology. Negative H_L anomalies leeward of the mountains (Figure 8c) indicate that the air is drier than the climatology and that sublimation occurs over Larsen C. Extremely positive sensible heat anomalies (Figure 8d) are modelled east of the mountain crest and extend across the ice shelf as foehn flow mixes warm, dry air towards the surface. H_S fluxes dominate the SEB during the three primary foehn events that occur during the period (Figure S5). This strong foehn effect generates mean E_{tot} anomalies (Figure 8e) of up to 76.8 W m^{-2} in the lee of the mountains. Mean E_{melt} anomalies (Figure 8f) of up to 61.1 W m^{-2} are simulated wherever E_{tot} is positive, as mean maximum air temperatures are above 0°C in almost all locations (Figure 8a). These modelled anomalies agree well with the observational and model data presented in Kuipers Munneke et al. (2018), which show that foehn events produced by the isentropic drawdown mechanism (Elvidge & Renfrew, 2016) delivered large sensible heat fluxes (up to 300 W m^{-2} in the strongest case) that were responsible for driving melting during May 2016. They are also in agreement with Datta et al. (2019) and Wiesenekker et al. (2019), which both show above-average foehn occurrence in March-May 2016.

Table 4. Mean modelled MAM foehn occurrence during the model hindcast period ("1998-2017 mean"), mean modelled MAM foehn occurrence during the hindcast period plus one standard deviation ("Mean + SD") and modelled foehn occurrence during MAM 2016 ("MAM 2016") at each station.

AWS	**1998-2017 mean (%)**	**Mean + SD (%)**	**MAM 2016 (%)**
AWS 14	13.9	17.6	22.8
AWS 15	10.3	13.5	18.3
AWS 17	15.7	19.3	21.5
AWS 18	15.1	18.9	24.2

Figure 9 shows that the associated E_{melt} anomalies result in anomalous cumulative meltwater production over Larsen C, with 29 times more melt (5.7 Gt) produced during the MAM 2016 season than in the 1998-2017 MAM climatology (0.2 Gt), representing 35.4% of the meltwater production for the 2015/16 melt year (August-July, 16.0 Gt). This value is consistent with the 23% of annual meltwater production reported by Kuipers Munneke et al. (2018) for the period January-December 2016. These results are also consistent with the results of Datta et al. (2019) who find elevated foehn occurrence and meltwater production during March and May 2016 compared with the 2016 annual mean.

The mean modelled MAM 2016 meltwater production anomaly over Larsen C relative to the model MAM climatology is shown in Figure 7b, with maximum simulated melt along a transect shown in Figure 9a. Maximum melt fluxes along the transect are highest in the immediate lee of the mountains, and diminish rapidly with distance from the peak of orography as warm, dry foehn air is increasingly mixed into cold ambient air. Regions of elevated melt exist further out onto the ice shelf in some regions, with "streams" of higher melt emanating from the mouths of inlets. The locations of these qualitatively match with the foehn "jet" regions identified by Elvidge et al. (2015), which are typically cooler but experience higher wind speeds during foehn events. They are downstream of mountain passes which channel the flows as “gap winds” and enhance the wind speed, but cause air to be sourced from lower altitude, meaning that it is cooler when it reaches the surface than in adjacent "wake" regions. Because the events during MAM 2016 are so intense and ambient temperatures are so high, the relatively cooler jet temperatures do not limit melting, and the elevated wind speeds enhance the sensible heat flux enough to drive extremely intense melting in these jet regions.

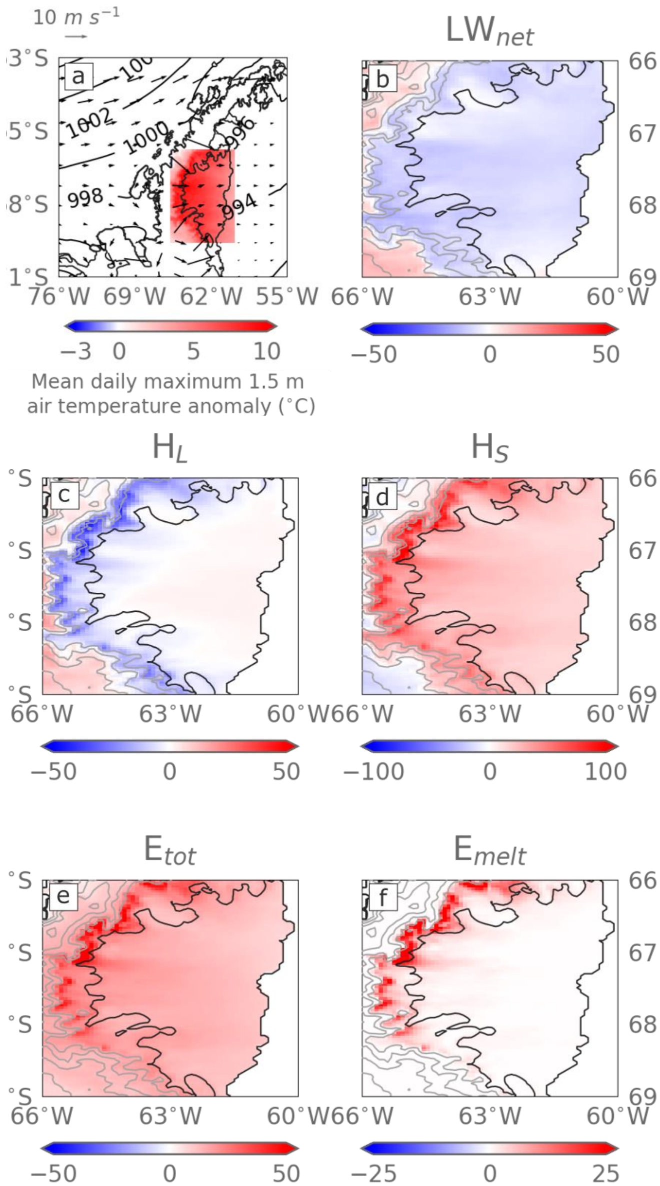

Figure 8. Mean modelled synoptic meteorological conditions and surface flux and temperature anomalies during 15 April – 31 May 2016. Panel a) shows mean modelled meteorological conditions, where colours indicate the mean daily maximum 1.5 m air temperature anomaly (in °C), contours show mean sea level pressure (hPa) and vectors show mean 10 m wind speed and direction. Panels b) to f) show flux anomalies, in W m^{-2}, of LW_{net}, H_L, H_S, E_{tot} and E_{melt}, respectively. In all panels the anomalies are calculated relative to the 1998-2017 model climatology for 15 April – 31 May. Blue colours indicate negative anomalies while red colours show positive anomalies.

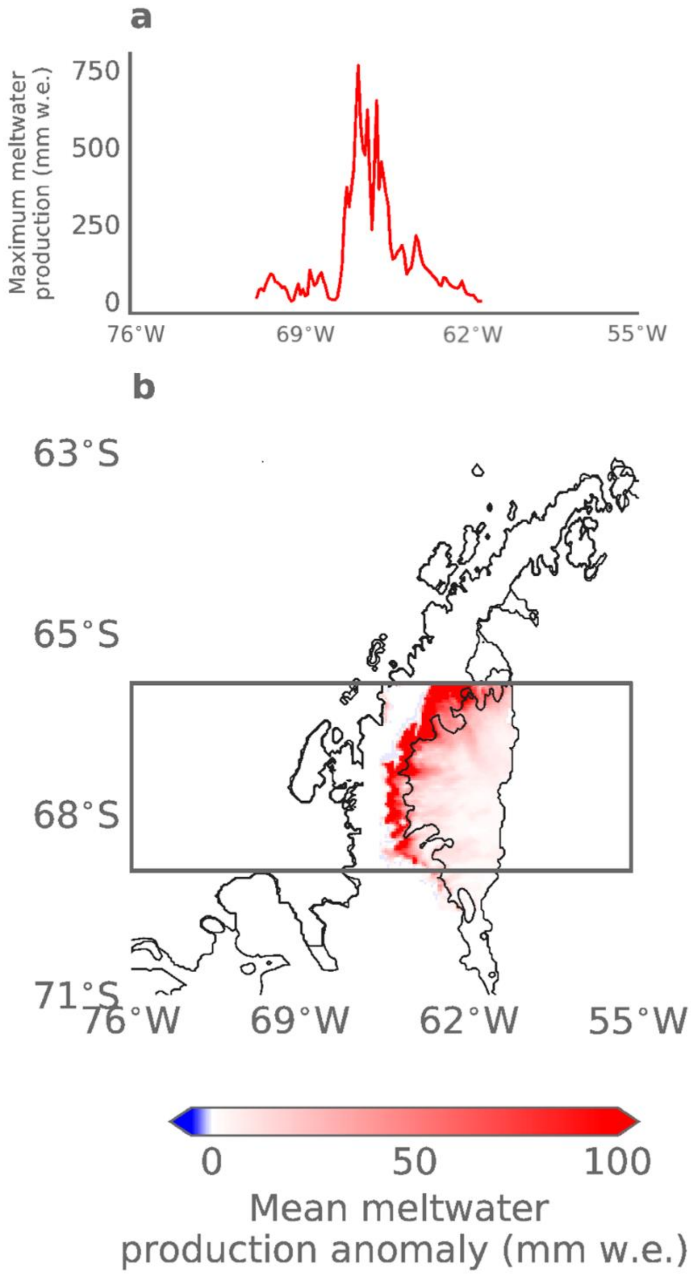

Figure 9. Mean meltwater production over Larsen C during 15 April – 31 May 2016. Panel a) shows the maximum cumulative melt produced along an east-west transect, indicated by the grey box in panel b). Panel b) shows the mean cumulative meltwater production anomaly with respect to the 1998-2017 model climatology for 15 April – 31 May.

4 Conclusions

The high-resolution regional model hindcast presented here is a novel dataset with which to evaluate meteorology, SEB and surface melt over the central Antarctic Peninsula. Visual inspection shows that the hindcast qualitatively reproduces the longitudinal and latitudinal gradients of surface melting on Larsen C identified from satellite observations, which are known to be linked to the north-south gradient in temperature and SW radiation and the east-west gradient in foehn wind occurrence. This multi-decadal hindcast of surface melt, meteorology and SEB builds on Elvidge et al. (2020), which uses a similar configuration of the MetUM to explain the influence of foehn winds on the SEB of Larsen C during a shorter six-month period.

By re-visiting a case study of the period immediately preceding the collapse of the Larsen B ice shelf, we show that the hindcast captures both the magnitude of surface melting observed on Larsen B prior to its collapse, and the driving meteorological conditions implicated in its disintegration.

Compared to other years in the hindcast, much higher foehn frequency was simulated in MAM 2016, consistent with Kuipers Munneke et al. (2018). Exceptionally high foehn occurrence in this season (more than two standard deviations above the mean at three of the four AWSs considered) produced very large sensible heat flux anomalies, which drove positive E_{tot} and E_{melt} fluxes. These results indicate that the large proportion of melt, 23%, observed in the period April-October (taken to be ‘winter’ in Kuipers Munneke et al., 2018) was much higher in 2016 than it has been in other years in the hindcast, providing a better ‘big picture’ context in which to view those results.

The hindcast results presented in this study build upon previous work that has attempted to quantify the patterns of surface melting on Larsen C (e.g. Elvidge et al., 2016; 2020; King et al., 2017; Turton et al., 2018; 2020; Weisenekker et al., 2019; Kirchgaessner et al., 2019; Datta et al., 2019; Laffin et al., 2021). These results advance our understanding by using a non-hydrostatic RCM at sufficiently high resolution to capture foehn winds, which are demonstrably important for determining surface melt. However, the configuration of the MetUM used in this study has relatively simplistic snow and albedo parameterisations compared to those used in the MAR and

RACMO models, which likely contributes to biases in the simulated SEB. Nevertheless, MAR and RACMO are hydrostatic and so simulate foehn flows less well, and hindcasts using these models have been used at coarser resolutions. Further development to implement more sophisticated schemes in the MetUM, such as the multi-layer snow model within the JULES land surface model (Walters et al., 2019) and prognostic albedo (Best et al., 2011) must therefore be a priority to address this limitation.

Part 2 of this study will further explore the causes and implications of surface melting on Larsen C. It will use the hindcast model output to identify the most important meteorological drivers of surface melting on Larsen C, specifically by quantifying the influence of foehn winds, cloud phase and large-scale circulation on the SEB.

Acknowledgments, Samples, and Data

The authors declare no conflicts of interest. This work was supported by the Natural Environment Research Council through the EnvEast Doctoral Training Partnership (grant number NE/L002582/1). The authors also acknowledge use of the MONSooN system, a collaborative facility supplied under the Joint Weather and Climate Research Programme, a strategic partnership between the Met Office and the Natural Environment Research Council. The authors gratefully acknowledge Prof. Michiel R. van den Broeke, who kindly provided AWS data. The manuscript was greatly improved by the comments of R. Tri Datta, J. Lenaerts and two anonymous reviewers.

Hindcast model data can be accessed on the CEDA archive at https://catalogue.ceda.ac.uk/uuid/41c879b06af642e9bc8e12d1d0ea3d62 and can be cited as Gilbert, E. (2020): High-resolution regional Met Office Unified Model (UM) climate model hindcast of the Antarctic Peninsula (1998-2017). Centre for Environmental Data Analysis, date of citation. AWS data can be retrieved from https://www.projects.science.uu.nl/iceclimate/aws/.

References

Bannister, D. (2015). Föhn winds on South Georgia and their impact on regional climate. PhD thesis, University of East Anglia.

Best, M. J., Pryor, M., Clark, D. B., Rooney, G. G., Essery, R. L. H., Menard, C. B., Edwards, J. M., Hendry, M. A., Porson, A., Gedney, N., Mercado, L. M., Sitch, S., Blyth, E., Boucher, O., Cox, P. M., Grimmond, C. S. B., and Harding, R. J. (2011). The joint UK Land Environment Simulator (JULES), model description – Part 1: energy and water fluxes. *Geoscientific Model Development*, 4, 677-699, https://doi.org/10.5194/gmd-4-677-2011.

Bevan, S., Luckman, A., Hubbard, B., Kulessa, B., Ashmore, D., Kuipers Munneke, P., O'Leary, M., Booth, A., Sevestre, H., & McGrath, D. (2017). Centuries of intense surface melt on Larsen C Ice Shelf. *The Cryosphere Discussions*, 1–21. https://doi.org/10.5194/tc-2017-81

Borstad, C. P., Rignot, E., Mouginot, J., & Schodlok, M. P. (2013). Creep deformation and buttressing capacity of damaged ice shelves: Theory and application to Larsen C ice shelf. *Cryosphere*, *7*(6), 1931–1947. https://doi.org/10.5194/tc-7-1931-2013

Bush, M., Allen, T., Bain, C., Boutle, I., Edwards, J., Finnenkoetter, A., Franklin, C., Hanley, K., Lean, H., Lock, A., Manners, J., Mittermaier, M., Morcrette, C., North, R., Petch, J., Short, C., Vosper, S., Walters, D., Webster, S., … Zerroukat, M. (2020). The first Met Office Unified

Model-JULES Regional Atmosphere and Land configuration, RAL1. *Geoscientific Model Development*, *13*, 1999–2029. https://doi.org/10.5194/gmd-13-1999-2020

Cape, M. R., Vernet, M., Skvarca, P., Marinsek, S., Scambos, T., & Domack, E. (2015). Foehn winds link climate-driven warming to ice shelf evolution in Antarctica. *Journal of Geophysical Research: Atmospheres*, *120*(21), 11037–11057. **https://doi.org/10.1002/2015JD023465**

Carrasco, J. F., Bozkurt, D., & Cordero, R. R. (2021). A review of the observed air temperature in the Antarctic Peninsula. Did the warming trend come back after the early 21st hiatus? *Polar Science, 2021* (in press). https://doi.org/10.1016/j.polar.2021.100653

Cook, A. J., & Vaughan, D. G. (2010). Overview of areal changes of the ice shelves on the Antarctic Peninsula over the past 50 years. *The Cryosphere Discussions*, *3*(2), 579–630. https://doi.org/10.5194/tcd-3-579-2009

Datta, R. T., Tedesco, M., Fettweis, X., Agosta, C., Lhermitte, S., Lenaerts, J. T. M., & Wever, N. (2019). The Effect of Foehn-Induced Surface Melt on Firn Evolution Over the Northeast Antarctic Peninsula. *Geophysical Research Letters*, *46*, 3822–3831. https://doi.org/10.1029/2018GL080845

Dee, D. P., Uppala, S. M., Simmons, A. J., Berrisford, P., Poli, P., Kobayashi, S., Andrae, U., Balmaseda, M. A., Balsamo, G., Bauer, P., Bechtold, P., Beljaars, A. C. M., van de Berg, L., Bidlot, J., Bormann, N., Delsol, C., Dragani, R., Fuentes, M., Geer, A. J., … Vitart, F. (2011). The ERA-Interim reanalysis: Configuration and performance of the data assimilation system.

Quarterly Journal of the Royal Meteorological Society, *137*(656), 553–597. https://doi.org/10.1002/qj.828

Dutra, E., Sandu, I., Balsamo, G., Beljaars, A., Freville, H., Vignon, E., & Brun, E. (2015). Understanding the ECMWF winter surface temperature biases over Antarctica. In *ECMWF Internal Report* (Vol. 762, Issue January 2016). https://doi.org/10.13140/RG.2.1.5165.5762

Elvidge, A. D., & Renfrew, I. A. (2016). The causes of foehn warming in the lee of mountains. *Bulletin of the American Meteorological Society*, *97*(3), 455–466. https://doi.org/10.1175/BAMS-D-14-00194.1

Elvidge, A. D., Renfrew, I. A., King, J. C., Orr, A., Lachlan-Cope, T. A., Weeks, M., & Gray, S. L. (2015). Foehn jets over the Larsen C Ice Shelf, Antarctica. *Quarterly Journal of the Royal Meteorological Society*, *141*(688), 698–713. https://doi.org/10.1002/qj.2382

Elvidge, A. D., Renfrew, I. A., King, J. C., Orr, A., & Lachlan-Cope, T. A. (2016). Foehn warming distributions in nonlinear and linear flow regimes: A focus on the Antarctic Peninsula. *Quarterly Journal of the Royal Meteorological Society*, *142*(695), 618–631. https://doi.org/10.1002/qj.2489

Elvidge, A. D., Kuipers Munneke, P., King, J. C., Renfrew, I. A., & Gilbert, E. (2020). Atmospheric Drivers of Melt on Larsen C Ice Shelf: Surface Energy Budget Regimes and the Impact of Foehn. *Journal of Geophysical Research: Atmospheres*, *125*(17). https://doi.org/10.1029/2020JD032463

Fréville, H., Brun, E., Picard, G., Tatarinova, N., Arnaud, L., Lanconelli, C., Reijmer, C., & Van Den Broeke, M. (2014). Using MODIS land surface temperatures and the Crocus snow model to understand the warm bias of ERA-Interim reanalyses at the surface in Antarctica. *Cryosphere*, *8*(4), 1361–1373. https://doi.org/10.5194/tc-8-1361-2014

Fürst, J. J., Durand, G., Gillet-chaulet, F., Tavard, L., Rankl, M., Braun, M., & Gagliardini, O. (2016). The safety band of Antarctic ice shelves. *Nature Climate Change*, *6*(February), 2014–2017. https://doi.org/10.1038/NCLIMATE2912

Gilbert, E. (2020) Atmospheric drivers of surface melting on the Larsen C ice shelf, Antarctic Peninsula. PhD thesis, University of East Anglia.

Gilbert, E., Orr, A., King, J. C., Renfrew, I. A., Lachlan-Cope, T., Field, P. F., & Boutle, I. A. (2020). Summertime cloud phase strongly influences surface melting on the Larsen C ice shelf, Antarctica. *Quarterly Journal of the Royal Meteorological Society*, *146*(729), 1575–1589. https://doi.org/10.1002/qj.3753

Holland, P. R., Corr, H. F. J., Pritchard, H. D., Vaughan, D. G., Arthern, R. J., Jenkins, A., & Tedesco, M. (2011). The air content of Larsen Ice Shelf. *Geophysical Research Letters*, *38*(10), 1–6. https://doi.org/10.1029/2011GL047245

Hersbach, H., Bell, B., Berrisford, P., Hirahara, S., Horányi, A., Muñoz-Sabater, J., Nicolas, J., Peubey, C., Radu, R., Schepers, D., Simmons, A., Soci, C., Abdalla, S., Abellan, X., Balsamo, G., Bechtold, P., Biavati, G., Bidlot, J., Bonavita, M., … Thépaut, J. N. (2020). The ERA5 global reanaly**sis. *Quarterly Journal of the Royal Meteorological Society*, *146*(730), 1999–2049. https://doi.org/10.1002/qj.3803**Hubbard, B., Luckman, A., Ashmore, D. W., Bevan, S., Kulessa, B., Kuipers Munneke, P., Philippe, M., Jansen, D., Booth, A., Sevestre, H., Tison, J.-L., O'Leary, M., & Rutt, I. (2016). Massive subsurface ice formed by refreezing of ice-shelf melt ponds. *Nature Communications*, *7*(May), 11897. https://doi.org/10.1038/ncomms11897

Khazendar, A., Rignot, E., & Larour, E. (2011). Acceleration and spatial rheology of Larsen C Ice Shelf , Antarctic Peninsula. *Geophysical Research Letters*, *38*(January), 1–5. https://doi.org/10.1029/2011GL046775

King, J. C., Kirchgaessner, A., Orr, A., Luckman, A., Bevan, S., Elvidge, A., Renfrew, I. A., & Kuipers Munneke, P. (2017). The impact of foehn winds on surface energy balance and melt over Larsen C Ice Shelf, Antarctica. *Journal of Geophysical Research: Atmospheres*, *122*(22), 12062–12076. https://doi.org/10.1002/2017JD026809

Kirchgaessner, A., King, J., & Gadian, A. (2019). The Representation of Föhn Events to the East of the Antarctic Peninsula in Simulations by the Antarctic Mesoscale Prediction System. *Journal of Geophysical Research: Atmospheres*, *124*(24), 13663–13679. https://doi.org/10.1029/2019JD030637

Kuipers Munneke, P., Ligtenberg, S. R. M., Van Den Broeke, M. R., & Vaughan, D. G. (2014). Firn air depletion as a precursor of Antarctic ice-shelf collapse. *Journal of Glaciology*, *60*(220), 205–214. https://doi.org/10.3189/2014JoG13J183

Kuipers Munneke, P., Van Den Broeke, M. R., King, J. C., Gray, T., & Reijmer, C. H. (2012). Near-surface climate and surface energy budget of Larsen C ice shelf, Antarctic Peninsula. *Cryosphere*, *6*(2), 353–363. https://doi.org/10.5194/tc-6-353-2012

Kuipers Munneke, P., van den Broeke, M. R., Reijmer, C. H., Helsen, M. M., Boot, W., Schneebeli, M., & Steffen, K. (2009). The role of radiation penetration in the energy budget of the snowpack at Summit, Greenland. *The Cryosphere*, *3*(1), 155–165. **https://doi.org/10.5194/tcd-3-277-2009**

Laffin, M. K., Zender, C. S., Singh, S., Van Wessem, J. M., Smeets, C. J. P. P., & Reijmer, C. H. (2021). Climatology and Evolution of the Antarctic Peninsula Föhn Wind-Induced Melt Regime

From 1979–2018. Journal of Geophysical Research: Atmospheres, 126(4), 1–19. **https://doi.org/10.1029/2020JD033682**

Liu, H., Jezek, K. C., Li, B., & Zhao, Z. (2015). *RadarSat Antarctic Mapping Project Digital Elevation Model, version 2*. NSIDC; NASA National Snow and Ice Data Center Distributed Active Archive Center. https://doi.org/https://doi.org/10.5067/8JKNEW6BFRVD

Luckman, A., Elvidge, A., Jansen, D., Kulessa, B., Kuipers Munneke, P., King, J., & Barrand, N. E. (2014). Surface melt and ponding on Larsen C Ice Shelf and the impact of föhn winds. *Antarctic Science*, *26*(6), 625–635. https://doi.org/10.1017/S0954102014000339

Orr, A., Hunt, J. C. R., Capon, R., Sommeria, J., Cresswell, D., & Owinoh, A. (2005). Coriolis effects on wind jets and cloudiness along coasts. *Weather*, *60*(10), 291–299.

Orr, A., Phillips, T., Webster, S., Elvidge, A., Weeks, M., Hosking, S., & Turner, J. (2014). Met Office Unified Model high-resolution simulations of a strong wind event in Antarctica. *Quarterly Journal of the Royal Meteorological Society*, *140*(684), 2287–2297. **https://doi.org/10.1002/qj.2296**

Orr, A. Kirchgaessner, A., King, J. C., Phillips, T., Gilbert, E., Elvidge, A., Weeks, M., Gadian, A., Kuipers Munneke, P., van den Broeke, M., Webster, S. & McGrath, D. (2021) Comparison of kilometre and sub-kilometre scale simulations of a foehn wind event over the Larsen C Ice

Shelf, Antarctic Peninsula using the Met Office Unified Model (MetUM). *Quarterly Journal of the Royal Meteorological Society.* Submitted**.**

Parish, T. R. (1983). The Influence of the Antarctic Peninsula on the Wind Field Over the Western Weddell Sea. Journal of Geophysical Research, 88(C4), 2684–2692. https://doi.org/10.1029/JC088iC04p02684

Rignot, E., Casassa, G., Gogineni, P., Krabill, W., Rivera, A., & Thomas, R. (2004). Accelerated ice discharge from the Antarctic Peninsula following the collapse of Larsen B ice shelf. *Geophysical Research Letters*, *31*(July), 2–5. https://doi.org/10.1029/2004GL020697

Rott, H., Rack, W., Skvarca, P., & De Angelis, H. (2002). Northern Larsen Ice Shelf, Antarctica: further retreat after collapse. *Annals of Glaciology*, *34*, 277–282. https://doi.org/https://doi.org/10.3189/172756402781817716

Rott, H., Skvarca, P., & Nagler, T. (1996). Rapid collapse of Northern Larsen ice shelf, Antarctica. *Science*, *271*(5250), 788–792. https://doi.org/10.1126/science.271.5250.788

Scambos, T. A., Bohlander, J. A., Shuman, C. A., & Skvarca, P. (2004). Glacier acceleration and thinning after ice shelf collapse in the Larsen B embayment, Antarctica. *Geophysical Research Letters*, *31*(18), 2001–2004. https://doi.org/10.1029/2004GL020670

Scambos, T. A., Hulbe, C., & Fahnestock, M. (2003). Climate-induced ice shelf disintegration in the Antarctic Peninsula. In E. Domack, A. Leventer, A. Burnet, R. Bindschadler, P. Convey, & M. Kirby (Eds.), *Antarctic Peninsula Climate Variability: Historical and Paleoenvironmental Perspectives* (Vol. 79, pp. 79–92). American Geophysical Union. https://doi.org/doi:10.1029/AR079p0079

Scambos, T. A., Hulbe, C., M.Fahnestock, & J.Bohlander. (2000). The link between climate warming and break-up of ice shelves in the Antarctica Peninsula. *Journal of Glaciology*, *46*(154), 516–530. https://doi.org/http://dx.doi.org/10.3189/172756500781833043

Sedlar, J., Tjernström, M., Rinke, A., Orr, A., Cassano, J., Fettweis, X., Heinemann, G., Seefeldt, M., Solomon, A., Matthes, H., Phillips, T., & Webster, S. (2020). Confronting Arctic Troposphere, Clouds, and Surface Energy Budget Representations in Regional Climate Models

With Observations. *Journal of Geophysical Research: Atmospheres*, *125*(6), 1–29. https://doi.org/10.1029/2019JD031783

Smeets, C. J. P. P. (2006). Assessing unaspirated temperature measurements using a thermocouple and a physically based model. The Mass Budget of Arctic Glaciers. Extended Abstracts, Workshop and GLACIODYN Planning Meeting, 29, 99–101. Available online at: https://webspace.science.uu.nl/~reijm101/publications/2006_abstracts_nag.pdf#page=100

Smeets, P. C. J. P., Kuipers Munneke, P., van As, D., van den Broeke, M. R., Boot, W., Oerlemans, H., Snellen, H., Reijmer, C. H., & van de Wal, R. S. W. (2018). The K-transect in west Greenland: Automatic weather station data (1993–2016). *Arctic, Antarctic, and Alpine Research*, *50*(1), e1420954. https://doi.org/10.1080/15230430.2017.1420954

Trusel, L. D., Frey, K. E., Das, S. B., Karnauskas, K. B., Kuipers Munneke, P., van Meijgaard, E., & van den Broeke, M. R. (2015). Divergent trajectories of Antarctic surface melt under two twenty-first-century climate scenarios. *Nature Geoscience*, *8*(12), 927–932. https://doi.org/10.1038/ngeo2563

Trusel, L. D., Frey, K. E., Das, S. B., Kuipers Munneke, P., & Van Den Broeke, M. R. (2013). Satellite-based estimates of Antarctic surface meltwater fluxes. *Geophysical Research Letters*, *40*(23), 6148–6153. https://doi.org/10.1002/2013GL058138

Turner, J., Lu, H., White, I., King, J. C., Phillips, T., Hosking, J. S., Bracegirdle, T. J., Marshall, G. J., Mulvaney, R., & Deb, P. (2016). Absence of 21st century warming on Antarctic Peninsula consistent with natural variability. Nature, 535(7612), 411–415. https://doi.org/10.1038/nature18645

Turton, J. V., Kirchgaessner, A., Ross, A. N., & King, J. C. (2018). The spatial distribution and temporal variability of föhn winds over the Larsen C ice shelf, Antarctica. *Quarterly Journal of the Royal Meteorological Society*, *144*(713), 1169–1178. **https://doi.org/10.1002/qj.3284**

Turton, J. V., Kirchgaessner, A., Ross, A., King, J., & Kuipers Munneke, P. (2020). The influence of föhn winds on annual and seasonal surface melt on the Larsen C Ice Shelf, Antarctica. *The Cryosphere* 14, 4165–4180. **https://doi.org/10.5194/tc-2020-72**

van den Broeke, M. (2005). Strong surface melting preceded collapse of Antarctic Peninsula ice shelf. *Geophysical Research Letters*, *32*, 2–5. https://doi.org/10.1029/2005GL023247

Van Wessem, J. M., Ligtenberg, S. R. M., Reijmer, C. H., Van De Berg, W. J., Van Den Broeke, M. R., Barrand, N. E., Thomas, E. R., Turner, J., Wuite, J., Scambos, T. A., & Van Meijgaard, E. (2016). The modelled surface mass balance of the Antarctic Peninsula at 5.5 km horizontal resolution. *The Cryosphere*, *10*(1), 271–285. https://doi.org/10.5194/tc-10-271-2016

Van Wessem, J. M., Reijmer, C. H., Van De Berg, W. J., Van Den Broeke, M. R., Cook, A. J., Van Ulft, L. H., & Van Meijgaard, E. (2015). Temperature and wind climate of the Antarctic Peninsula as simulated by a high-resolution Regional Atmospheric Climate Model. *Journal of Climate*, *28*(18), 7306–7326. https://doi.org/10.1175/JCLI-D-15-0060.1

Walters, D., Boutle, I., Brooks, M., Melvin, T., Stratton, R., Vosper, S., Wells, H., Williams, K., Wood, N., Allen, T., Bushell, A., Copsey, D., Earnshaw, P., Edwards, J., Gross, M., Hardiman, S., Harris, C., Heming, J., Klingaman, N., … Xavier, P. (2017). The Met Office Unified Model Global Atmosphere 6.0/6.1 and JULES Global Land 6.0/6.1 configurations. *Geoscientific Model Development*, *10*(4), 1487–1520. https://doi.org/10.5194/gmd-10-1487-2017

Wang, W., Zender, C. S., Van As, D., Smeets, P. C. J. P., & Van Den Broeke, M. R. (2016). A Retrospective, Iterative, Geometry-Based (RIGB) tilt-correction method for radiation observed by automatic weather stations on snow-covered surfaces: Application to Greenland. *Cryosphere*, *10*(2), 727–741. https://doi.org/10.5194/tc-10-727-2016

Wiesenekker, J. M., Kuipers Munneke, P., van den Broeke, M. R., & Smeets, P. C. J. P. (2018). A multidecadal analysis of Föhn winds over Larsen C ice shelf from a combination of observations and modeling. *Atmosphere*, *9*(5). https://doi.org/10.3390/atmos9050172

Wood, N., & Mason, P. (1993). The Pressure force induced by neutral, turbulent flow over hills. *Quarterly Journal of the Royal Meteorological Society*, *119*(514), 1233–1267. https://doi.org/10.1002/qj.49711951402

Wood, N., Staniforth, A., White, A., Allen, T., Diamantakis, M., Gross, M., Melvin, T., Smith, C., Vosper, S., Zerroukat, M., & Thuburn, J. (2014). An inherently mass-conserving semi-implicit semi-Lagrangian discretization of the deep-atmosphere global non-hydrostatic equations. *Quarterly Journal of the Royal Meteorological Society*, *140*(682), 1505–1520. https://doi.org/10.1002/qj.2235